Pergamon

Acta Materialia 50 (2002) 395–411

Acta MATERIALIA

www.elsevier.com/locate/actamat

# Effect of substrate constraint on the stability and evolution of ferroelectric domain structures in thin films

Y.L. Li, S.Y. Hu, Z.K. Liu, L.Q. Chen *

*Department of Materials Science and Engineering, The Pennsylvania State University, University Park, PA 16802, USA*

Received 11 July 2001; received in revised form 6 September 2001; accepted 6 September 2001

**Abstract**

The stability and evolution of ferroelectric domain structures in thin films are studied. Elastic solutions are derived for both elastically anisotropic and isotropic thin films with arbitrary domain structures, subject to the mixed stress-free and constraint boundary conditions. These solutions are employed in a three-dimensional phase-field model to investigate simultaneously the effect of substrate constraint and temperature on the volume fractions of domain variants, domain-wall orientations, surface topology, domain shapes, and their temporal evolution for a cubic-to-tetragonal ferroelectric phase transition. A specific example of a [001] orientated film heteroepitaxially grown on a [001] cubic substrate is considered. It is shown that the shapes of *a*-domains with tetragonal axes parallel to the film surface are significantly different from those of *c*-domains with tetragonal axes perpendicular to the film surface. For the substrate constraints and temperatures under which both *a*- and *c*-domains coexist, both types of *a*-domains are present with their tetragonal axes perpendicular to each other, and the domain wall orientations deviate from the 45 orientation generally assumed in thermodynamic analyses. It is demonstrated that a substrate constraint results in sequential nucleation and growth of different tetragonal domains during a ferroelectric phase transition. 

*Keywords:* Ferroelectric domain structure; Thin films; Computer simulation

## 1. Introduction

Ferroelectrics are a class of materials possessing a spontaneous polarization that can be reoriented between crystallographically defined states in a single crystal by an electric field [1,2]. A common feature for ferroelectric materials is the formation of domain structures when a paraelectric phase is cooled through the ferroelectric transition temperature, also known as the Curie temperature. Each individual domain is a microscopic region with uniform electrical polarization. The crystallography and thermodynamics of domain structures in bulk systems have been extensively studied and reasonably well understood [3]. For example, in a cubic to tetragonal transformation, there are three possible orientation variants with the tetragonal axes along the [100], [010], and [001] directions of the cubic paraelectric phase. In the absence of

* Corresponding author. Tel.: +1-814-863-8101; fax: +1-814-865-0016.

*E-mail address:* Lqc3@psu.edu (L.Q. Chen).

1359-6454/02/$22.00 
PII: S1359-6454(01)00360-3

any external field or constraint, all of them have the same probability to form in a parent phase below the ferroelectric transition temperature. The corresponding domain structure of the ferroelectric phase will contain all possible orientations of domains with statistically equal volume fractions, separated by the so-called domain walls. In such a system, there are two types of special domain walls: the 180 walls separating domains with opposite directions of polarization, and the 90 walls separating domains with perpendicular directions of polarization. The stability and orientations of the domain walls are determined by minimizing the sum of the electrostatic energy, the elastic energy, and the wall energy of a domain structure.

The domain configurations in ferroelectrics could be dramatically changed by external constraints. For ferroelectric thin films constrained by a substrate, the existence of a free surface and substrate constraint destroys the macroscopic symmetry of the system and can significantly affect both the Curie temperature and the relative volume fractions of domains with different orientations [4–15]. Thanks to the recent advances in theories of ferroelectric domains, it is now possible to construct domain stability maps which show the volume fractions of domains as a function of lattice mismatch with substrate and/or temperature [4,11–15]. However, in order to determine the volume fractions of domains that minimize the total free energy at a given temperature and substrate constraint, a simple domain structure with a particular domain wall orientation is usually assumed as a priori. For example, essentially all existing thermodynamic models of tetragonal ferroelectric domain structures on a [001] cubic substrate considered only two types of tetragonal domains, forming essentially a two dimensional (2D) domain structure (Fig. 1). In a three-dimensional (3D) film, depending on the degree of substrate constraint, all three types of tetragonal domains may co-exist and the domain structure can be much more complicated.

To study the stability and evolution of 3D ferroelectric domain structures in a thin film constrained by a substrate, we adopted a phase-field approach. The phase-field approach has previously been applied to modeling microstructure evolution during structural transformations in bulk systems (see [16] for references), including domain structure evolution during a ferroelectric phase transition in bulk single crystals [17–19]. The presence of a stress-free surface and substrate constraint for a thin film requires a significantly different elastic solution from bulk systems. In this work, we derived elastic solutions for thin films containing arbitrary distributions of domains for both the elastically anisotropic and isotropic systems by combining the Khachaturyan's mesoscopic elasticity theory [20,21] and the Stroh formalism of anisotropic elasticity [22,23]. The elastic solutions are then incorporated in a phase-field model for predicting the domain structures in constrained 3D ferroelectric thin films. Such an approach does not make any a priori assumptions with regard to the possible domain structures that might appear under a given temperature and substrate constraint. It is able to predict not only the effect of substrate constraint on phase transition temperatures and the volume fractions of orientation domains, but also the detailed domain structures and their temporal evolution during a ferroelectric transition. It will be shown that the domain shapes and domain wall configurations in constrained film can be significantly more complicated than those assumed in prior thermodynamic analysis. We will show that the substrate constraint not only affects ferroelectric transition temperatures and domain volume fractions, but also significantly alters the domain evolution path during a ferroelectric phase transition. The results are compared with existing experimental observations and prior thermodynamic analyses. The validity of the assumption of

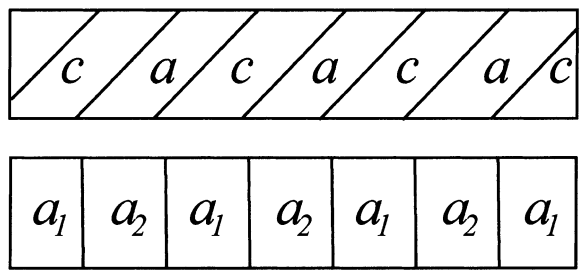


Fig. 1. Schematic illustrations on the 2D representation of 3D thin film domain structures: (a) *c*/*a*/*c*/*a* domain structure; (b) $a_1/a_2/a_1/a_2$ domain structure.

isotropic elasticity and a 2D representation of 3D domain structures are discussed.

## 2. Phase field model of a ferroelectric film

We consider a cubic thin film grown heteroepitaxially on a cubic substrate. The film undergoes cubic→tetragonal ferroelectric phase transitions when it is cooled below the Curie temperature. For a proper ferroelectric phase transition, the polarization vector $\mathbf{P}=(P_1, P_2, P_3)$ is the primary order parameter, and its spatial distribution in the ferroelectric state describes a domain structure.

The temporal evolution of the polarization field, and thus the domain structure evolution, is described by the Time Dependent Ginzburg–Landau (TDGL) equations,

$$\frac{\partial P_i(\mathbf{x},t)}{\partial t} = -L\frac{\delta F}{\delta P_i(\mathbf{x},t)}, \ (i = 1,2,3), \tag{1}$$

where $L$ is the kinetic coefficient, and $F$ is the total free energy of the system. $\delta F/\delta P_i(\mathbf{x},t)$ is the thermodynamic driving force for the spatial and temporal evolution of $P_i(\mathbf{x},t)$. The total free energy of the system includes the bulk free energy, the domain wall energy, the elastic energy, the surface and interface contributions, and the depolarization energy. In this work, we ignore any possible surface and interface contributions to the free energy as discussed in Refs. 24 and 25, and assume that the film's surface is compensated with free charge carriers so the depolarization energy is neglected.

To solve Eq. (1), one has to formulate the total free energy functional, $F$, in terms of the polarization field variables, $P_1$, $P_2$ and $P_3$. We assume the transition, in the absence of substrate constraint, is first-order, and its bulk thermodynamics is characterized by the following Landau free energy density expansion [26],

$$\begin{aligned} f_L(P_i) \ &= \alpha_1(P_1^2 + P_2^2 + P_3^2) + \alpha_{11}(P_1^4 + P_2^4 + P_3^4) + \alpha_{12}(P_1^2P_2^2 + P_2^2P_3^2 + P_1^2P_3^2) \\ &\quad + \alpha_{111}(P_1^6 + P_2^6 + P_3^6) \\ &\quad + \alpha_{112}[P_1^4(P_2^2 + P_3^2) + P_2^4(P_1^2 + P_3^2) + P_3^4(P_1^2 + P_2^2)] + \alpha_{123}(P_1^2P_2^2P_3^2), \end{aligned} \tag{2}$$

where $\alpha_1$, $\alpha_{11}$, $\alpha_{12}$, $\alpha_{111}$, $\alpha_{112}$, $\alpha_{123}$ are the expansion coefficients. The values of these coefficients determine the thermodynamic behavior of the bulk paraelectric and ferroelectric phases as well as the bulk ferroelectric properties, such as the ferroelectric transition temperature, the stability and metastability of the parent paraelectric phase, the spontaneous polarization and the susceptibility as functions of temperature, etc. For example, $\alpha_1 = 1/2\varepsilon_0\chi$, where $\varepsilon_0$ is the vacuum permittivity, and $\chi$ is the susceptibility of the material. A negative value for $\alpha_1$ corresponds to an unstable parent paraelectric phase with respect to its transition to the ferroelectric state. A positive $\alpha_1$ value indicates either a stable or metastable parent phase, depending on the relations among $\alpha_1$, $\alpha_{11}$ and $\alpha_{111}$. If $\alpha_{11}^2 > 3\alpha_1\alpha_{111}$, the parent phase is metastable, otherwise it is stable.

The contribution of domain walls to the total free energy, i.e. the domain wall energy, is introduced through the gradients of the polarization field. For a cubic system, the gradient energy density has the following expression:

$$\begin{aligned} f_G(P_{i,j}) \ &= \frac{1}{2}G_{11}(P_{1,1}^2 + P_{2,2}^2 + P_{3,3}^2) + G_{12}(P_{1,1}P_{2,2} + P_{2,2}P_{3,3} + P_{1,1}P_{3,3}) \\ &\quad + \frac{1}{2}G_{44}[(P_{1,2} + P_{2,1})^2 + (P_{2,3} + P_{3,2})^2 + (P_{1,3} + P_{3,1})^2] \\ &\quad + \frac{1}{2}G'_{44}[(P_{1,2} - P_{2,1})^2 + (P_{2,3} - P_{3,2})^2 + (P_{1,3} - P_{3,1})^2], \end{aligned} \tag{3}$$

where $G_{ij}$ are gradient energy coefficients. In this paper, a comma in a subscript stands for spatial differentiation, for example, $P_{i,j} = \partial P_i/\partial x_j$. In general, the domain wall energy is anisotropic.

Since the proper ferroelectric phase transition involves structural changes, strain appears as a secondary order parameter. The stress-free strain caused by the polarization field is given by [26]

$$\begin{aligned} \varepsilon_{11}^o &= Q_{11}P_1^2 + Q_{12}(P_2^2 + P_3^2), \\ \varepsilon_{22}^o &= Q_{11}P_2^2 + Q_{12}(P_1^2 + P_3^2), \\ \varepsilon_{33}^o &= Q_{11}P_3^2 + Q_{12}(P_1^2 + P_2^2), \\ \varepsilon_{23}^o &= Q_{44}P_2P_3, \\ \varepsilon_{13}^o &= Q_{44}P_1P_3, \\ \varepsilon_{12}^o &= Q_{44}P_1P_2, \end{aligned} \tag{4}$$

where $Q_{ij}$ are the electrostrictive coefficients. If we assume that the interfaces developed during a fer-

roelectric phase transition as well as the interface between the film and the substrate are coherent, elastic strains will be generated during the phase transition in order to accommodate the structural changes. They are given by

$$e_{ij} = \varepsilon_{ij} - \varepsilon^o_{ij}, \tag{5}$$

where $\varepsilon_{ij}$ are the total strains. The corresponding elastic strain energy density can be expressed as

$$\begin{aligned} f_E &= \frac{1}{2} c_{ijkl} e_{ij} e_{kl} = \frac{1}{2} c_{ijkl} (\varepsilon_{ij} - \varepsilon^o_{ij})(\varepsilon_{kl} - \varepsilon^o_{kl}) \\ &= f_E(P_i, \varepsilon_{ij}), \end{aligned} \tag{6}$$

where $c_{ijkl}$ is the elastic stiffness tensor. The summation convention for the repeated indices is employed, and the Latin letters $i$, $j$, $k$, $l$ take 1,2,3 in this paper. For a cubic material with its three independent elastic constants $C_{11}$, $C_{12}$ and $C_{44}$ in the Voigt's notation, the elastic energy can be rewritten as

$$\begin{aligned} f_E &= \frac{1}{2} C_{11}(e_{11}^2 + e_{22}^2 + e_{33}^2) \\ &+ C_{12}(e_{11}e_{22} + e_{22}e_{33} + e_{11}e_{33}) \\ &+ 2C_{44}(e_{12}^2 + e_{23}^2 + e_{13}^2), \end{aligned} \tag{7}$$

which can be separated into three contributions,

$$f_E = f_{E1} + f_{E2} + f_{E3} \tag{8}$$

with

$$\begin{aligned} f_{E1} &= \frac{1}{2} C_{11}(\varepsilon_{11}^2 + \varepsilon_{22}^2 + \varepsilon_{33}^2) \\ &+ C_{12}(\varepsilon_{11}\varepsilon_{22} + \varepsilon_{22}\varepsilon_{33} + \varepsilon_{11}\varepsilon_{33}) \\ &+ 2C_{44}(\varepsilon_{12}^2 + \varepsilon_{23}^2 + \varepsilon_{13}^2), \end{aligned} \tag{9}$$

$$\begin{aligned} f_{E2} &= \beta_{11}(P_1^4 + P_2^4 + P_3^4) + \beta_{12}(P_1^2P_2^2 \\ &+ P_2^2P_3^2 + P_1^2P_3^2), \end{aligned} \tag{10}$$

$$\begin{aligned} f_{E3} = {} & -(q_{11}\varepsilon_{11} + q_{12}\varepsilon_{22} + q_{12}\varepsilon_{33})P_1^2 - (q_{11}\varepsilon_{22} + q_{12}\varepsilon_{11} + q_{12}\varepsilon_{33})P_2^2 \\ & -(q_{11}\varepsilon_{33} + q_{12}\varepsilon_{11} + q_{12}\varepsilon_{22})P_3^2 - 2q_{44}(\varepsilon_{12}P_1P_2 + \varepsilon_{23}P_2P_3 + \varepsilon_{13}P_2P_3), \end{aligned} \tag{11}$$

where

$$\begin{aligned} \beta_{11} &= \frac{1}{2} C_{11}(Q_{11}^2 + 2Q_{12}^2) + C_{12}Q_{12}(2Q_{11} \\ &+ Q_{12}), \\ \beta_{12} &= C_{11}Q_{12}(2Q_{11} + Q_{12}) + C_{12}(Q_{11}^2 \\ &+ 3Q_{12}^2 + 2Q_{11}Q_{12}) + 2C_{44}Q_{44}^2, \\ q_{11} &= C_{11}Q_{11} + 2C_{12}Q_{12}, \\ q_{12} &= C_{11}Q_{12} + C_{12}(Q_{11} + Q_{12}), \\ q_{44} &= 2C_{44}Q_{44}. \end{aligned}$$

From the above, it can easily been seen that the elastic energy contribution can alter the Landau's coefficients. In particular, with the elastic strain energy contribution, the second-order coefficient, $\alpha_1$, depends on $\varepsilon_{ij}$. Therefore, the thermodynamic stability of the paraelectric and ferroelectric phases can be modified by a substrate constraint. In addition, the introduction of elastic energy may change the characteristics, or the order, of a phase transformation by changing the sign of the fourth-order coefficients in the Landau expression, i.e. $\alpha_{11}$ and $\alpha_{12}$.

The total free energy of a film is the sum of the Landau free energy $F_L$, the domain wall energy $F_G$, and the elastic energy $F_E$:

$$\begin{aligned} F &= F_L(P_i) + F_G(P_{i,j}) + F_E(P_i, \varepsilon_{ij}) \\ &= \iiint_V [f_L(P_i) + f_G(P_{i,j}) \\ &+ f_E(P_i, \varepsilon_{ij})] d^3x, \end{aligned} \tag{12}$$

where $V$ is the volume of the film. In this expression, although the strain field $\varepsilon_{ij}$ appears as an order parameter in addition to the polarization field, one can assume that the system reaches its mechanical equilibrium instantaneously for a given polarization field distribution, because the mechanical relaxation of an elastic deformation is much faster than the relaxation of a polarization field. This assumption enables us to eliminate the strain field using the static condition of mechanical equilibrium. Therefore, the elastic strain energy of the film becomes a function of the polarization field. The calculation of the equilibrium elastic strain for a thin film with a stress-free surface and a substrate constraint is described in the following section.

## 3. Elastic field in a constrained film

We consider a thin film with its top surface stress-free and the bottom surface coherently con-

strained by the substrate (Fig. 2(a)). Within the film, there is an eigenstrain distribution, $\varepsilon^o_{ij}(\mathbf{x})$, describing the crystallographic relationship between a parent phase and a product phase for a structural phase transition. The rectangular coordinates $\mathbf{x}=(x_1, x_2, x_3)$ are originated at the interface, and $x_1$=[100], $x_2$=[010], $x_3$=[001]. In the linear elasticity, the stress $\sigma_{ij}$ is related to the elastic strain $e_{ij}$ by the Hooke's law:

$$\sigma_{ij} = c_{ijkl}e_{kl} = c_{ijkl}(\varepsilon_{kl}-\varepsilon^o_{kl}), \tag{13}$$

The mechanical equilibrium equations of the film are expressed as

$$\sigma_{ij,j} = 0. \tag{14}$$

The stress-free boundary condition at the top surface is given by

$$\sigma_{i3}|_{x_3 = h_f} = 0, \tag{15}$$

where $h_f$ is the film thickness (see Fig. 2(a)).

We separate the total strain of the film into a sum of a homogeneous strain $\bar{\varepsilon}_{ij}$ and a heterogeneous strain $\eta_{ij}(\mathbf{x})$, i.e.

$$\varepsilon_{ij}(\mathbf{x}) = \bar{\varepsilon}_{ij} + \eta_{ij}(\mathbf{x}). \tag{16}$$

Consequently, the stress is rewritten as

$$\sigma_{ij}(\boldsymbol{x}) = \bar{\sigma}_{ij} + s_{ij}(\boldsymbol{x}) \tag{17}$$

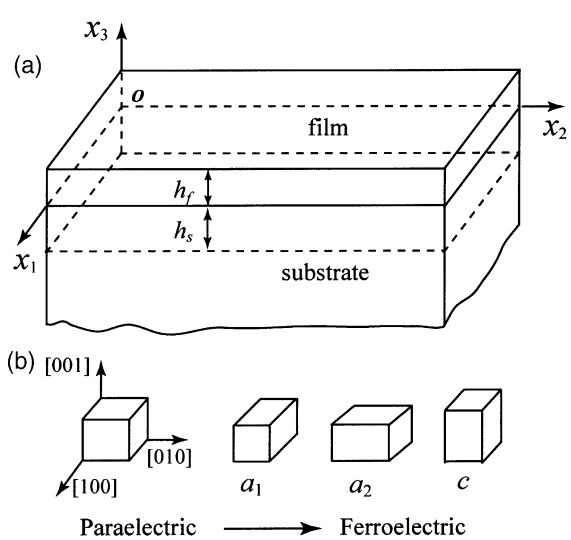


Fig. 2. Schematic illustrations of: (a) a thin film coherently constrained by a substrate, and (b) cubic paraelectric phase and the three ferroelectric tetragonal variants.

with

$$\bar{\sigma}_{ij}(\mathbf{x}) = c_{ijkl}\bar{\varepsilon}_{kl},\ s_{ij}(\mathbf{x}) = c_{ijkl}[\eta_{kl}(\mathbf{x})-\varepsilon^o_{kl}(\mathbf{x})].$$

Let $\bar{\varepsilon}_{\alpha\beta}$ $(\alpha,\beta = 1,2)$ represent the macroscopic shape deformation of the film in the film plane, we then have

$$\iiint_V \eta_{\alpha\beta}(\mathbf{x})d^3x = 0. \tag{18}$$

If the thin film is coherent with the substrate, the macroscopic shape deformation of the film in the film plane, $\bar{\varepsilon}_{\alpha\beta}$, is totally controlled by the sufficiently thick substrate. For example, for a cubic substrate of lattice parameter $\alpha_s$, and a thin film with a stress-free lattice parameter $a_f$, $\bar{\varepsilon}_{\alpha\beta}$ is given by $\bar{\varepsilon}_{11} = \bar{\varepsilon}_{22} = (a_s-a_f)/a_s$, $\bar{\varepsilon}_{12} = 0$. The macroscopic shape deformation of the film along $x_3$ is determined by both the substrate constraint and the domain structure in the film. Here, we choose the quantity $\bar{\varepsilon}_{i3}$ of Eq. (16) in such a way that it makes $c_{i3kl}\bar{\varepsilon}_{kl} = 0$. It should be pointed out that $\bar{\varepsilon}_{i3}$ thus obtained is only part of the total shape deformation of the film.

In order to solve the heterogeneous strain, $\eta_{ij}$, we introduce a set of displacements $u_i(\mathbf{x})$,

$$\eta_{ij} = \frac{1}{2}(u_{i,j} + u_{j,i}). \tag{19}$$

The equations of equilibrium (14) are thus rewritten as

$$c_{ijkl}u_{k,lj} = c_{ijkl}\varepsilon^o_{ki,j}, \tag{20}$$

and the boundary condition (15) on the top surface changes to

$$c_{i3kl}(u_{k,l}-\varepsilon^o_{kl})|_{x_3 = h_f} = 0. \tag{21}$$

Since the elastic perturbation resulted from the heterogeneous strain $\eta_{ij}$ disappears in the substrate far from the film–substrate interface, one can use the following condition

$$u_i|_{x_3 = -h_s} = 0 \tag{22}$$

to replace the constraint of the substrate. In Eq. (22), $h_s$ is the distance from the film–substrate

interface into the substrate, beyond which the elastic deformation is ignored (see Fig. 2(a)).

For the sake of simplicity, the elastic properties of the film and the substrate are assumed to be the same although the elastic anisotropy can be arbitrary. We take two steps to solve Eqs. (20)–(22). First, we use Khachaturyan's elasticity theory [20,21] to solve Eq. (20) in a 3D space with eigenstrain distribution $\varepsilon^o_{ij}$ within $0<x_3<h_f$. The corresponding solution labelled by superscript $A$ is given by

$$u^A_i(\mathbf{x}) = \int\int\int_{-\infty}^{\infty} \hat{u}^A_i(\boldsymbol{\zeta}) e^{I\mathbf{x}\cdot\boldsymbol{\zeta}} d^3\zeta, \qquad (23)$$

$$\hat{u}^A_i = -Ig_{ij}c_{jmkl}\hat{\varepsilon}^o_{kl}\zeta_m,$$

where $I=\sqrt{-1}$,

$$\hat{\varepsilon}^o_{ij}(\boldsymbol{\zeta}) = \frac{1}{(2\pi)^3}\int\int\int_{-\infty}^{\infty} \varepsilon^o_{ij}(\mathbf{x}) e^{-I\mathbf{x}\cdot\boldsymbol{\zeta}} d^3x, \qquad (24)$$

$g=(g_{ij})$ is the inverse tensor to $g^{-1}=(g^{-1}_{ij})$, $g^{-1}_{ij}=c_{ikjl}\zeta_k\zeta_l$, $\boldsymbol{\zeta}=(\zeta_1,\zeta_2,\zeta_3)$ is the coordinate in the Fourier space, and $d^3\zeta = d\zeta_1 d\zeta_2 d\zeta_3$.

The next step is to find an elastic solution labelled by superscript $B$, i.e. $u^B_i$, in an infinite plate of thickness $h_f + h_s$, satisfying the equation of equilibrium without body-force, i.e.

$$c_{ijkl}u^B_{k,lj} = 0, \qquad (25)$$

with the following boundary conditions:

$$c_{i3kl}u^B_{k,l}|_{x_3=h_f} = -c_{i3kl}(u^A_{k,l}-\varepsilon^o_{kl})|_{x_3=h_f}, \qquad (26)$$
$$u^B_i|_{x_3=-h_s} = -u^A_i|_{x_3=-h_s}.$$

To solve Eq. (25) with the boundary conditions (26), we make use of 2D Fourier transforms,

$$\hat{u}^B_i(\zeta_1,\zeta_2,x_3) = \frac{1}{(2\pi)^2}\int_{-\infty}^{\infty}\int_{-\infty}^{\infty} u^B_i(x_1,x_2,x_3) e^{-I(\zeta_1x_1+\zeta_2x_2)} dx_1\, dx_2. \qquad (27)$$

Eq. (25) in Fourier space is given by Ref. 27

$$c_{i\alpha k\beta}(I\zeta_\alpha)(I\zeta_\beta)\hat{u}^B_k + (c_{i\alpha k3} + c_{i3k\alpha})(I\zeta_\alpha)\hat{u}^B_{k,3} + c_{i3k3}\hat{u}^B_{k,33} = 0, \qquad (28)$$

where the summations over repeated $\alpha$ and $\beta$ are from 1 to 2. If we let $\zeta=\sqrt{\zeta_1^2+\zeta_2^2}$, then a general solution to Eq. (28) is

$$\hat{\mathbf{u}}^B(\zeta_1,\zeta_2,x_3) = \mathbf{a}e^{Ip\zeta x_3}, \qquad (29)$$

where $\hat{\mathbf{u}}^B=(\hat{u}^B_1,\hat{u}^B_2,\hat{u}^B_3)^T$, $p$ and $\mathbf{a}=(a_1,a_2,a_3)^T$ satisfy the eigenrelation [23]

$$\{W + p(R+R^T) + p^2U\}\mathbf{a} = \mathbf{0}, \qquad (30)$$

with $W_{ik}=c_{ijkl}n_jn_l$, $R_{ik}=c_{ijkl}n_jm_l$, $U_{ik}=c_{ijkl}m_jm_l$, $\mathbf{m}=(0,0,1)^T$, $\mathbf{n}=(n_1,n_2,0)^T$, $n_1=\zeta_1/\zeta$, $n_2=\zeta_2/\zeta$. The superscript $T$ stands for the transpose of matrices or vectors. The matrices $W$ and $U$ are symmetric and positive definite. Eq. (30) can be rewritten in a standard eigenrelation [23]

$$N\boldsymbol{\xi} = p\boldsymbol{\xi},\ N=\begin{pmatrix} N_1 & N_2 \\ N_3 & N_1^T\end{pmatrix},\ \boldsymbol{\xi}=\begin{pmatrix}\mathbf{a}\\ \mathbf{b}\end{pmatrix}, \qquad (31)$$

with $N_1=-U^{-1}R^T$, $N_2=U^{-1}$, $N_3=RU^{-1}R^T-W$, $\mathbf{b}=(R^T+pU)\mathbf{a}=-(W+pR)\mathbf{a}/p$. $U^{-1}$ is the inverse matrix of $U$. It can be easily shown that the heterogeneous stress $\hat{\mathbf{s}}^B=(\hat{s}^B_{13},\hat{s}^B_{23},\hat{s}^B_{33})^T$, is related to the vector $\mathbf{b}$ through $\hat{\mathbf{s}}^B = I\zeta\mathbf{b}e^{IP\zeta x_3}$.

The eigenvalue $p$ and the associated eigenvector $\boldsymbol{\xi}$ from Eq. (31) are complex, and each appears as three complex conjugate pairs. We use $p_t$ and $\boldsymbol{\xi}_t$ ($t$=1,2,…,6) to represent the six eigenvalues and eigenvectors which are arranged such that the imaginary part of $p_t$ is greater than zero for $t$=1,2,3, and $p_{t+3}=\bar{p}_t$, $\boldsymbol{\xi}_{t+3}=\bar{\boldsymbol{\xi}}_t$, where the overbar denotes the complex conjugate.

If matrix $N$ is simple or semisimple, i.e. Eq. (31) possesses six independent eigenvectors, the general solution for $\hat{\mathbf{u}}^B$ can be obtained by superposing the six independent solution of Eq. (29):

$$\hat{\mathbf{u}}^B(\zeta_1,\zeta_2,x_3) = \sum_{t=1}^{6} q_t\mathbf{a}_t e^{Ip_t\zeta x_3}, \qquad (32)$$

where $q_t$ ($t$=1,2,…,6) are unknown constants. They can be determined from boundary conditions (26) in their 2D Fourier transforms.

If $N$ is a non-semisimple matrix, i.e. there are less than six independent eigenvectors, the solution in Eq. (32) needs to be modified. Anisotropic elastic materials for which $N$ is non-semisimple are called degenerate materials. Isotropic materials are a special group of degenerate materials for which

$p = I$ is an eigenvalue of multiplicity three but there are only two independent eigenvectors for $\boldsymbol{\xi}$. Here we present a solution to the degenerate case that $\underline{p}_3 = \underline{p}_2$ and $\boldsymbol{\xi}_3 = \boldsymbol{\xi}_2$ (thus, $p_6 = \bar{p}_3 = \bar{p}_2 = p_5$, $\boldsymbol{\xi}_6 = \boldsymbol{\xi}_3 = \boldsymbol{\xi}_2 = \boldsymbol{\xi}_5$:

$$\begin{aligned}\hat{\mathbf{u}}^B = & \sum_{t=1,2,4,5} q_t \mathbf{a}_t e^{Ip_t\zeta x_3} \\ & + q_3'[\mathbf{a}_3' e^{Ip_3\zeta x_3} + I\zeta x_3 \mathbf{a}_2 e^{Ip_3\zeta x_3}] \\ & + q_6'[\mathbf{a}_6' e^{\mathbf{I}p_6\zeta x_3} + I\zeta x_3 \mathbf{a}_5 e^{Ip_6\zeta x_3}],\end{aligned} \tag{33}$$

where $\boldsymbol{\xi}_3' = (\mathbf{a}_3', \mathbf{b}_3')^T$ is determined by

$$N\boldsymbol{\xi}_3' = p_2\boldsymbol{\xi}_3' + \boldsymbol{\xi}_2. \tag{34}$$

If we use $\mu$ and $\nu$ to represent the shear modulus and Poisson's ratio for an elastically isotropic material, the corresponding eigenvalues and eigenvectors in Eq. (33) are given by

$$p_1 = p_2 = p_3 = I, p_4 = p_5 = p_6 = -I, \tag{35}$$

$$\begin{aligned}\boldsymbol{\xi}_1 &= \left(-\frac{In_2}{\mu n_1}, \frac{I}{\mu}, 0, -\frac{n_2}{n_1}, 1, 0\right)^T, & \boldsymbol{\xi}_4 &= \bar{\boldsymbol{\xi}}_1, \\ \boldsymbol{\xi}_2 &= \left(-\frac{In_1}{4\mu\nu}, -\frac{In_2}{4\mu\nu}, -\frac{1}{4\mu\nu}, -\frac{n_1}{2\nu}, -\frac{n_2}{2\nu}, \frac{I}{2\nu}\right)^T, & \boldsymbol{\xi}_5 &= \bar{\boldsymbol{\xi}}_2, \\ \boldsymbol{\xi}_3' &= \left(\frac{1-2\nu}{2\mu\nu n_1}, 0, \frac{I}{4\mu\nu}, -\frac{I(1-2\nu)}{2\nu n_1}, 0, 1\right)^T, & \boldsymbol{\xi}_6' &= \bar{\boldsymbol{\xi}}_3'.\end{aligned} \tag{36}$$

Substituting Eqs. (35) and (36) into Eq. (33), we obtain the solution for the elasticially isotropic materials. It is exactly the same as that directly obtained for isotropic materials [28] and was employed in our earlier work on ferroelectric domains in thin films [29].

The displacement field $u_i^B$ in the real space $\mathbf{x} = (x_1, x_2, x_3)$ can be obtained from Eq. (32) or Eq. (33) through an inverse Fourier transform,

$$u_i^B(x_1, x_2, x_3) = \int_{-\infty}^{\infty}\int_{-\infty}^{\infty} \hat{u}_i^B(\zeta_1, \zeta_2, x_3) e^{I(\zeta_1 x_1 + \zeta_2 x_2)} d\zeta_1\, d\zeta_2. \tag{37}$$

The sum of solutions $A$ and $B$, i.e.

$$u_i(\mathbf{x}) = u_i^A(\mathbf{x}) + u_i^B(\mathbf{x}) \tag{38}$$

yields the solution for the boundary value problem of Eqs. (20)–(22). The total strain and stress can be calculated by Eqs. (16), (17) and (19). Consequently, the elastic energy can be obtained for a thin film with an arbitrary eigenstrain distribution.

## 4. Numerical simulations

The temporal evolution of the polarization vector fields, and thus the domain structures, are obtained by numerically solving the TDGL Eq. (1). In this work, we used the semi-implicit Fourier-spectral method [30] for the time-stepping and spatial discretization.

We use lead titanate ($PbTiO_3$) thin film as an example for the numerical simulation. The corresponding material constants for the Landau free energy, the electrostrictive coefficients and elastic properties are from the literature [31,32]: $\alpha_1$=3.8($T$−479)×10$^5$ C$^{-2}$ m$^2$ N, $\alpha_{11}$=−7.3×10$^7$ C$^{-4}$ m$^6$ N, $\alpha_{12}$=7.5×10$^8$ C$^{-4}$ m$^6$ N, $\alpha_{111}$=2.6×10$^8$ C$^{-6}$ m$^{10}$ N, $\alpha_{112}$=6.1×10$^8$ C$^{-6}$ m$^{10}$ N, $\alpha_{123}$=−3.7×10$^9$ C$^{-6}$ m$^{10}$ N, $Q_{11}$=0.089 C$^{-2}$ m$^4$, $Q_{12}$=−0.026 C$^{-2}$ m$^4$, $Q_{44}$=0.03375 C$^{-2}$ m$^4$, $C_{11}$=1.746×10$^{11}$ N m$^{-2}$, $C_{12}$=7.937×10$^{10}$ N m$^{-2}$, $C_{44}$=1.111×10$^{11}$ N m$^{-2}$, where $T$ is temperature in °C.

In the computer simulations, we employed 128×128×36 discrete grid points, and periodic boundary conditions are applied along the $x_1$ and $x_2$ axes. The grid spacing in real space is chosen to be $\Delta x_1/l_0 = \Delta x_2/l_0 = 1.0$ and $\Delta x_3/l_0 = 0.5$, where $l_0 = \sqrt{G_{110}/\alpha_0}$ and $\alpha_0 = |\alpha_1|_{T=25°C}$. We choose the gradient energy coefficients as $G_{11}/G_{110}$=0.6, $G_{12}/G_{110}$=0.0, $G_{44}/G_{110} = G_{44}'/G_{110} = 0.3$. The corresponding width of domain wall is about $1.5\Delta x_1$, and the domain wall energy densities at $T$=25°C are evaluated to be about $0.60\alpha_0 l_0 P_0^2$ for 90° domain walls and $1.26\alpha_0 l_0 P_0^2$ for 180° domain walls. $P_0 = |\mathbf{P}|_{T=25°C} = 0.757$ C m$^{-2}$ is the spontaneous polarization. If $l_0$=1.0 nm, $G_{110}$=1.73×10$^{-10}$ C$^{-2}$ m$^4$ N, and the domain wall energy density is about 0.06 N m$^{-1}$ for 90° domain wall, and the width of domain walls is around 1.5 nm, which is consistent with existing experimental measurements [8]. The time step for integration is $\Delta t/t_0$=0.06, where $t_0 = 1/(\alpha_0 L)$.

The degree of substrate constraint is measured

by the average strain $\bar{\varepsilon}_{\alpha\beta}$ ($\alpha/\beta$=1,2), i.e. the mismatch strain between the film and the substrate, and the substrate thickness $h_s$ beyond which the deformation in the substrate is ignored. For simplicity, we considered the case of $\bar{\varepsilon}_{11} = \bar{\varepsilon}_{22} = \bar{\varepsilon}$ and $\bar{\varepsilon}_{12} = 0$. Under such a constraint, there are three tetragonal variants with their tetragonal axes parallel to $x_1$[100], $x_2$[010] and $x_3$[001]. They are labelled $a_1$, $a_2$ and $c$ by the conventional notation, i.e. the tetragonal axis of $a_1$-variant is parallel to [100], $a_2$ to [010], $c$ to [001] (see Fig. 2(b)).

### 4.1. Effect of substrate deformation

We first studied the effect of $h_s$, on the volume fractions of the three different orientation domains and the domain morphology. The value of $h_s$ represents the region of the substrate that is allowed to deform, and thus to a certain degree, it represents the rigidity of the substrate. For example, $h_s$=0 represents a complete rigid substrate. The deformation of the substrate results from the heterogeneous deformation within the thin film, thus the displacements in the substrate should be zero at a distance sufficiently far away from the interface. Therefore, as $h_s$ increases, the results on the equilibrium domain structures, including the domain volume fractions, should converge. We considered a particular case of $\bar{\varepsilon} = -0.002$, a compressive mismatch, at $T$=25°C and $h_f$=20$\Delta x_3$. The formation of ferroelectric domains in the film is simulated for $h_s$=0.2$\Delta x_3$, 4$\Delta x_3$,…,12$\Delta x_3$. In each case, we started with a high-temperature paraelectric state and quenched it to 25°C. Ferroelectric domains nucleate, grow, and coarsen during annealing. In this section, we are focused on the effect of substrate constraint on the domain volume fractions and domain shapes. We calculated the volume fractions of $a_1$-, $a_2$-, and $c$-domains, $V_{a1}$, $V_{a2}$, and $V_c$, from the simulated domain structures at late stages of the evolution process, during which the domain volume fractions are close to the equilibrium values. Table 1 shows the domain volume fractions as functions of $h_s$. The remainder, $1-V_c-V_{a1}-V_{a2}$, is considered as the volume fraction of domain walls. It can be seen from Table 1 that $c$-domains dominate under the compressive mismatch. As expected, $V_c$ varies with $h_s$ and approaches a constant value as $h_s$ becomes larger.

We also examined the effect of $h_s$ on the domain wall orientations and the domain shapes. Shown in Fig. 3 are the 2D sections of domain structures consisting of only $c$- and $a_2$-domains cut at the same position for different values of $h_s$ (the white strips are $a_2$-domains, the gray regions alternating with the $a_2$-domains are $c$-domains, and the black bottom is the substrate). It is shown that for $h_s$=0.0, the width of $a_2$-domains becomes significantly smaller close to the film–substrate interface. Even with a relatively large value of $h_s$, the width of $a_2$-domains is slightly smaller at the film–substrate interface than that close to the surface. Therefore, the domain-wall orientation between $a_2$-domain and $c$-domain is not exactly 45° from the film–substrate interface. The domain shapes practically do not change when $h_s$ exceeds about half of the film thickness.

### 4.2. Effect of substrate constraint on domain volume fractions and domain morphology

We studied the effect of the mismatch strain 5 on the volume fractions of domains and domain morphology at $T$=25°C. Elastic deformation in the substrate is allowed by choosing a value of $h_s$=12$\Delta x_3$=0.6$h_f$. The volume fractions of the three tetragonal variants, as functions of the mismatch strain $\bar{\varepsilon}$ are given in Table 2. It is shown that the mismatch strain can dramatically alter the volume fractions of different orientation domains. Under a large compressive constraint, only $c$-domains exist. A typical domain structure with only $c$-domains is shown in Fig. 4(a). As the magnitude of $\bar{\varepsilon}$ increases (i.e. the magnitude of compressive strain decreases), the $a_1$- and $a_2$-domains start to appear, and the volume fraction of $c$-domains decreases, and thus the equilibrium domain structures consist of all three types of domains. A representative domain structure with small volume fractions of $a_1$- and $a_2$-domains is shown in Fig. 4(b). The $a_1$- and $a_2$-domains alternately insert into $c$-domains in platelet shapes, and align along [100] or [010] directions. The orientations of the domain walls between $a_1$- and $c$-domains or between $a_2$- and $c$-domains deviate slightly from the 45° directions

Table 1
Volume fractions $V_{a1}$, $V_{a2}$ and $V_c$ as functions of $h_s$

| $h_s$ | $0\Delta x_3$ | $2\Delta x_3$ | $4\Delta x_3$ | $6\Delta x_3$ | $8\Delta x_3$ | $10\Delta x_3$ | $12\Delta x_3$ |
|---|---|---|---|---|---|---|---|
| $V_{a1}$ | 0.073 | 0.083 | 0.088 | 0.100 | 0.104 | 0.106 | 0.110 |
| $V_{a2}$ | 0.060 | 0.065 | 0.071 | 0.077 | 0.080 | 0.085 | 0.088 |
| $V_c$ | 0.826 | 0.816 | 0.805 | 0.785 | 0.778 | 0.770 | 0.763 |

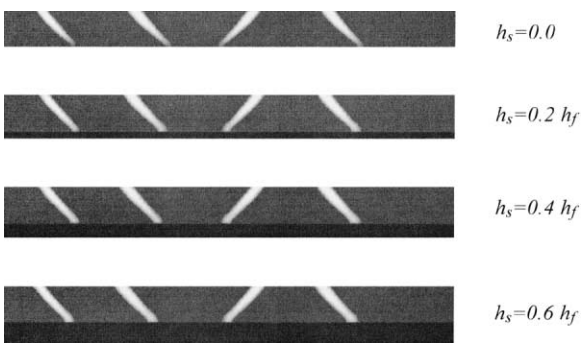


Fig. 3. Cross-section domain structures showing the dependence of the $a_2$-domain shapes on $h_s$.

from the film–substrate interface. The volume fractions of $a_1$- and $a_2$-domains have approximately the same value for a particular $\bar{\varepsilon}$ and increase with $\bar{\varepsilon}$. For comparison, a domain structure with a large volume fraction of *a*-domains ($a_1$+$a_2$) is presented in Fig. 4(c). There are no *c*-domains when $\bar{\varepsilon}$~0.010 or larger and only $a_1$- and $a_2$-domains exist (Fig. 4(d)). All the domain walls between $a_1$- and $a_2$-domains are perpendicular to the film surface and along the [110] or [1$\bar{1}$0] directions.

The pictures of domain shapes presented in Figs. 3 and 4 do not take into account the local displacements. As a result of domain formation, an initially atomically flat surface is expected to become rough. The surface topology change due to the domain formation can be automatically determined from the elastic solutions for a given domain structure. Fig. 5 shows an example of the displacements along the $x_3$ direction on the surface for the domain structure shown in Fig. 4(b). As expected, the displacements within the *c*-domains along the $x_3$ direction are significantly larger than those for the *a*-domains. Shown in Fig. 6 is a local cross-section for revealing the topology changes at the surface simply due to the displacements (see Fig. 3 at $h_s$=0.6$h_f$ for the corresponding domain structure). Particularly, it is shown that the surface of the *a*-domain has a slope about 3.7° from the horizontal direction, which agrees remarkably well with the experimental observation [33]. The direction of the tilt for the surface of an *a*-domain depends on the domain-wall orientation (see Fig. 6 for the difference in surface slopes between the two *a*-domains).

### 4.3. The domain stability map

We constructed a domain stability map by modelling the domain formation as a function of both substrate constraint and temperature. The results were summarized in Fig. 7. All the data points shown in Fig. 7 were obtained by starting from an initial paraelectric state with small random perturbations. The data points simply represent the type of domain structures that existed at the end of a simulation. Because of the numerical nature of the calculations, the lines which separate the stability

Table 2
Volume fractions $V_{a1}$, $V_{a2}$ and $V_c$ as functions of $\bar{\varepsilon}$

| $\bar{\varepsilon}$ | −0.010 | −0.008 | −0.006 | −0.004 | −0.002 | 0.000 | 0.002 | 0.004 | 0.006 | 0.008 | 0.010 |
|---|---|---|---|---|---|---|---|---|---|---|---|
| $V_{a1}$ | 0.000 | 0.002 | 0.024 | 0.066 | 0.110 | 0.143 | 0.201 | 0.263 | 0.354 | 0.452 | 0.468 |
| $V_{a2}$ | 0.000 | 0.004 | 0.027 | 0.055 | 0.088 | 0.139 | 0.188 | 0.256 | 0.344 | 0.452 | 0.468 |
| $V_c$ | 0.991 | 0.980 | 0.928 | 0.853 | 0.763 | 0.667 | 0.544 | 0.403 | 0.204 | 0.007 | 0.000 |

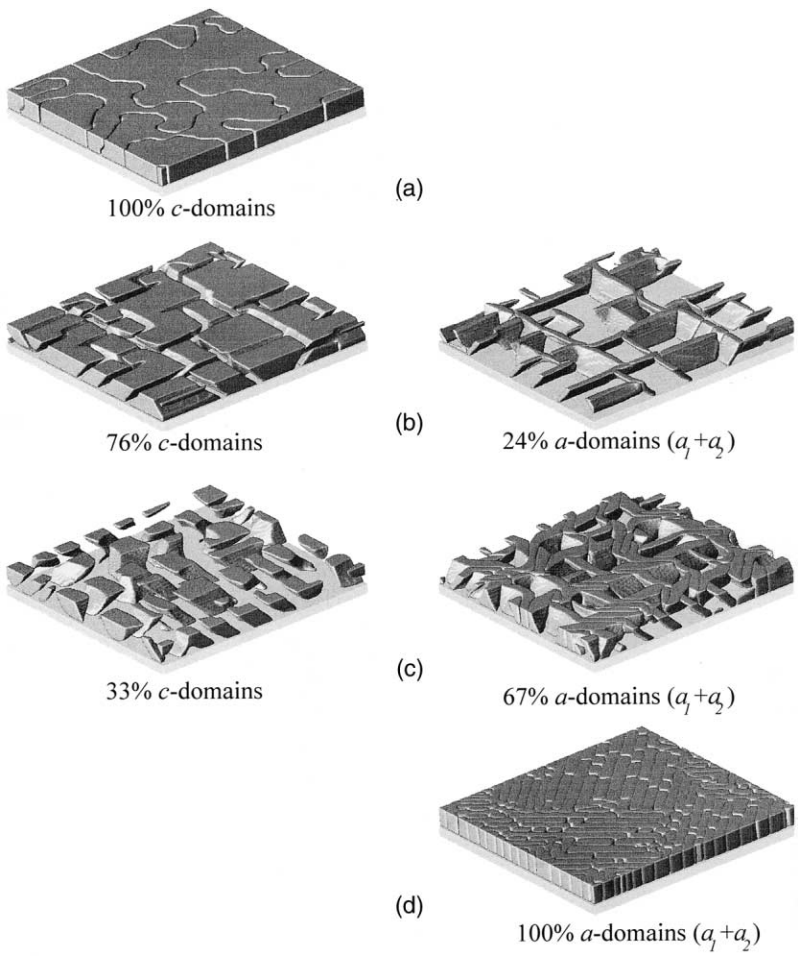


Fig. 4. Domain structures at 25°C: (a) *c*-domains ($\bar{\varepsilon} = -0.012$); (b) $c/a_1/a_2$ domain structure with 76% of *c*-domains ($\bar{\varepsilon} = -0.002$); (c) $c/a_1/a_2$ domain structure with 33% of *c*-domains ($\bar{\varepsilon} = 0.005$); (d) $a_1/a_2$ domain structure ($\bar{\varepsilon} = 0.012$).

of different types of domain structures cannot be determined exactly, i.e. they can only be determined approximately. For a given temperature, the equilibrium domain structures are a single *c*-domain state, a $c/a_1/a_2$ three-domain state, and $a_1/a_2$ two-domain state, as the substrate constraint changes from compressive to tensile.

The two lines in Fig. 7 represent the transition temperature of a paraelectric phase into a single *c*-domain or a single *a*-domain determined by assuming a bulk single crystal under an external constraint equal to the film–substrate lattice mismatch. The equations for the two lines are described by

$$\alpha_0 \frac{T-479}{454} - \left[ -2q_{11}\frac{C_{12}}{C_{11}} + 2q_{12} \right] \bar{\varepsilon} = 0 \qquad (39)$$

for the single *c*-domain state, and

$$\alpha_0 \frac{T-479}{454} - \left[ q_{11} + q_{12}\left(1 - 2\frac{C_{12}}{C_{11}}\right) \right] \bar{\varepsilon} = 0 \qquad (40)$$

for a single $a_1$- or $a_2$-domain state. Our computer simulations showed that the two lines are actually very good approximations of the paraelectric→ferroelectric transition temperatures in the thin films. As has been shown before [4,11–15], the substrate constraint can substantially increase the ferroe-

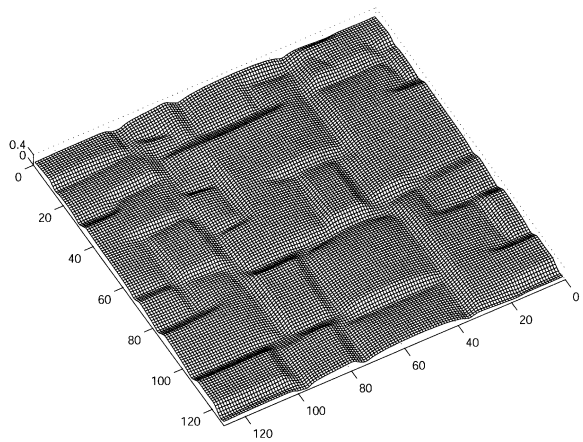

Fig. 5. Displacement pattern of the $x_3$ component on the surface.

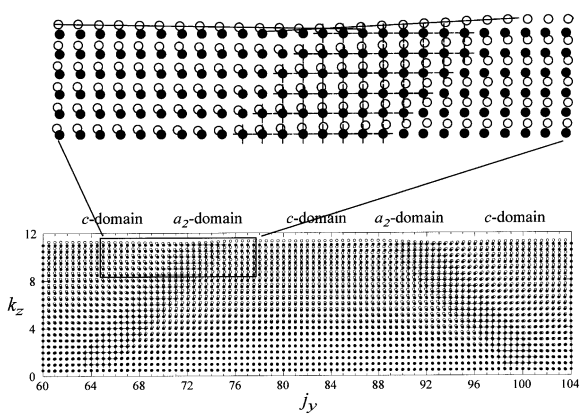


Fig. 6. A local cross-section showing the surface topology due to the domain formation. The surface of the *a*-domain has a slope about 3.7° from the horizontal direction. The solid circles represent the regular grid points. The grid points with both the plus sign and the solid circles are occupied by the $a_2$-domains. The open circles represent the deformed grid points, and hence the distances from the solid circles to the corresponding open circles are the magnitude of local displacements.

lectric transition temperature regardless of whether the constraint is compressive or tensile.

### 4.4. Temporal domain evolution

One of the advantages of the phase-field approach is that it allows one to follow the temporal evolution of ferroelectric domains during

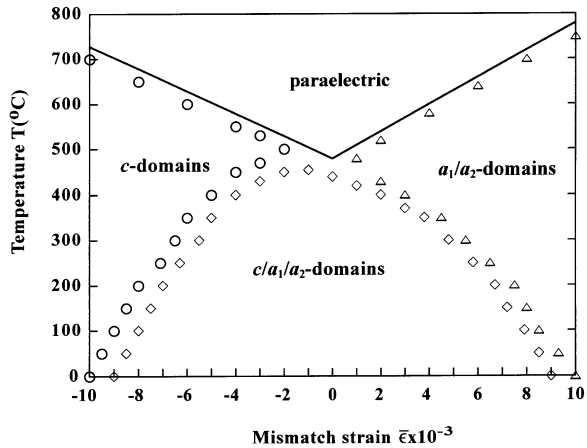


Fig. 7. The domain stability map of a film. The equilibrium phases or domain structures as a function of temperature and substrate constraint, obtained from phase-field simulations assuming coherent interface between the film and the substrate.

annealing of a quenched paraelectric phase below the ferroelectric transition temperature. Figs. 8–10 show three examples for the temporal evolution of the domain structures at three different substrate constraints, $\bar{\varepsilon} = -0.002$, 0.005 and 0.012, respectively, at $T$=25°. The domain structures are represented by the iso-surface with $P_i^* = |P_i|/P_0 = 0.6$. The evolutions of *a*- and *c*-domains are presented in separate pictures. However, the $a_1$-domains and $a_2$-domains are not distinguished in the pictures showing the evolution of *a*-domains, so plots of iso-surface only reveal the domain walls. In each case, the initial condition is a homogeneous paraelectric phase, created by assigning a zero value at each lattice site for each component of the polarization field plus a small random noise.

Fig. 8 shows the temporal evolution of domains under a compressive strain, −0.002. The initial paraelectric phase is unstable with respect to the formation of ferroelectric domains and hence homogeneous nucleation takes place. It is shown that the *c*-domains appear before the *a*-domains during the evolution process. The shape of *a*-domains is plate-like with the domain walls aligned about 45° from the substrate. Thermodynamically, it is rather easy to understand the sequential appearance of *c*- and *a*-domains since the substrate constraint favors the formation of *c*-domains over *a*-domains.

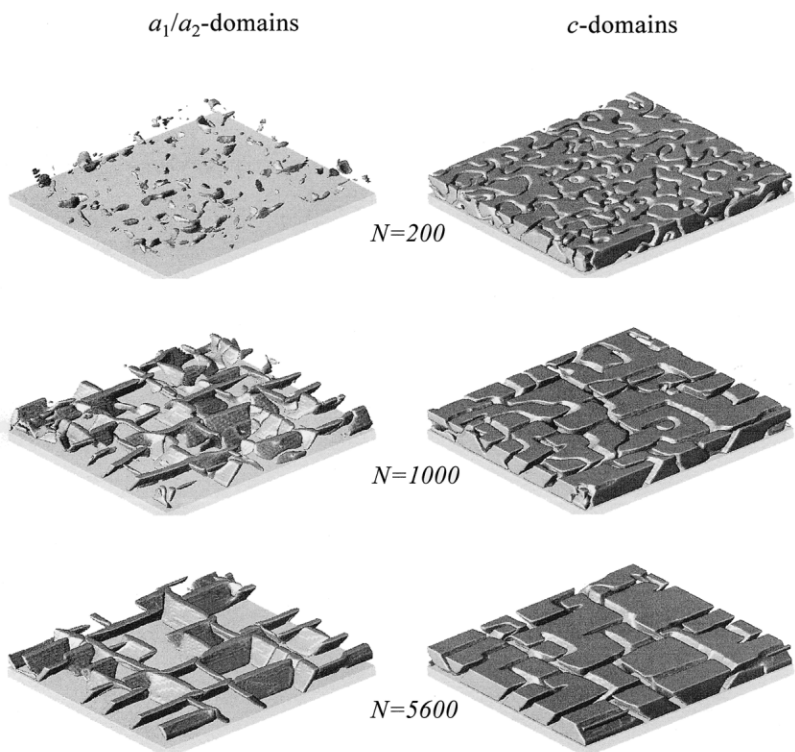


Fig. 8. Temporal evolution of ferroelectric domain morphologies at $\bar{\varepsilon} = -0.002$, $t=N\Delta t$.

In contrast to the compressive constraint, a tensile substrate constraint completely changes the sequence of appearance of *c*- and *a*-domains during the ferroelectric phase transition (Figs. 9 and 10), i.e. a tensile constraint increases the thermodynamic driving force for the formation of *a*-domains and decreases that for *c*-domains. In addition, there is clear evidence that the *c*-domains prefer nucleation near the surface. When $\bar{\varepsilon} = 0.012$, no *c*-domain exists. All the domain walls between $a_1$ and $a_2$ domains are perpendicular to the film surface and along the [110] or [1$\bar{1}$0] directions.

To verify the sequential nucleation and growth of different domains, the volume fractions versus time steps are plotted in Fig. 11 for the two cases, $\bar{\varepsilon} = -0.002$, 0.005. For the case of $\bar{\varepsilon} = -0.002$, the *a*-domain starts to appear after the volume fraction of *c*-domains almost reaches its equilibrium value, whereas for the case of $\bar{\varepsilon} = 0.005$, the *c*-domains nucleate after the formation of *a*-domains.

### *4.5. Discussion*

We showed above that a substrate constraint may drastically affect not only the volume fractions, but also the sequence of the nucleation and growth of different domains at a given temperature. The results obtained in this work on the dependence of domain volume fractions on the degree of substrate constraint qualitatively confirmed prior thermodynamic analyses, i.e. a compressive substrate constraint favors the formation of *c*-domains while a tensile substrate constraint makes the $a_1$- and $a_2$-domains more stable than the *c*-domains. Moreover, similar to the prior thermodynamic analyses, our results show that the ferroelectric transition temperature depends strongly on the substrate constraint. The domain morphologies obtained from our simulation for small volume fractions of $a_1$- and $a_2$-domains also agree very

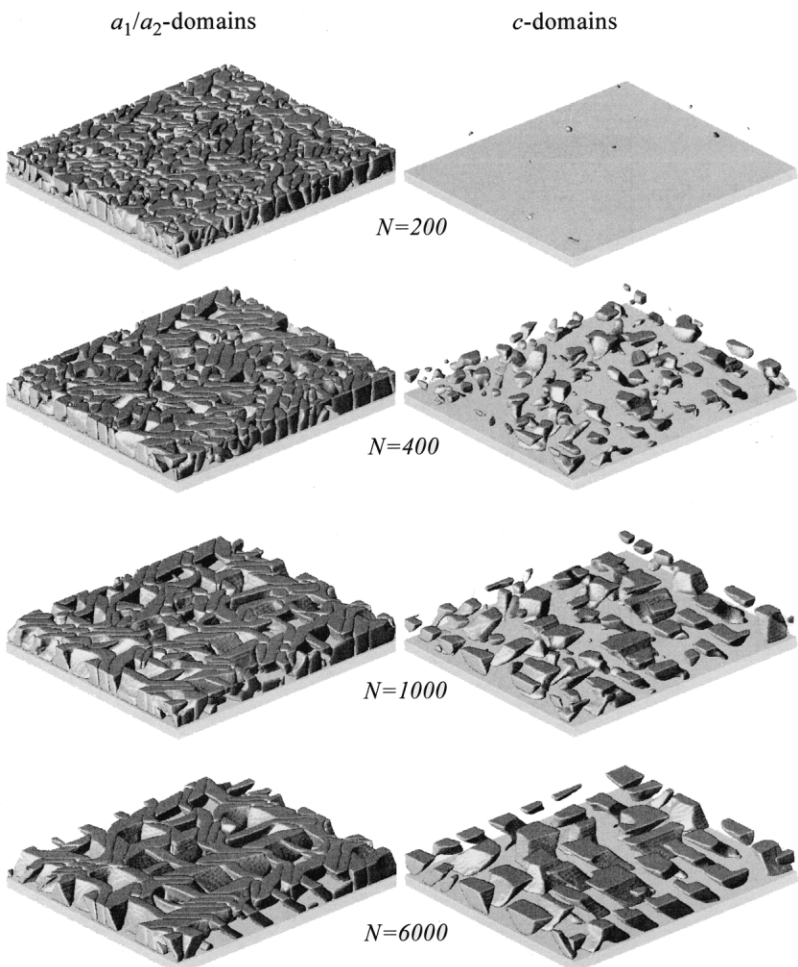


Fig. 9. Temporal evolution of ferroelectric domain morphologies at $\bar{\varepsilon} = -0.005$, $t = N\Delta t$.

well with existing experimental observations [5,7,33,34].

It should be emphasized that the phase-field approach presented here is 3D and does not make any a priori assumption on the possible domain wall orientations for predicting the domain structures. On the other hand, essentially all prior thermodynamic analyses consider only 2D domain structures (Fig. 1) and almost invariably assumed that the shapes of both the *a*- and *c*-domains are plates oriented 45° from the film–substrate interface. Therefore, there are a number of significant differences between prior thermodynamic predictions and the present phase-field simulations. First of all, the $a_1/a_2$ domain configurations under a large tensile mismatch (Figs. 4(d) and 8) were automatically predicted starting from an initial paraelectric state, whereas in the thermodynamic analysis, a domain configuration consisting of distorted orthorhombic phases was obtained under a similar tensile mismatch with the assumption of domain wall 45 inclined to the film–substrate interface [13]. In a more recent work [14,15], by assuming that the domain walls between $a_1$- and $a_2$-domains are perpendicular to the film–substrate interface, the same $a_1/a_2$ domain configuration was predicted as in our phase-field simulation. Second, our results show that $a_1$- and $a_2$-domains always

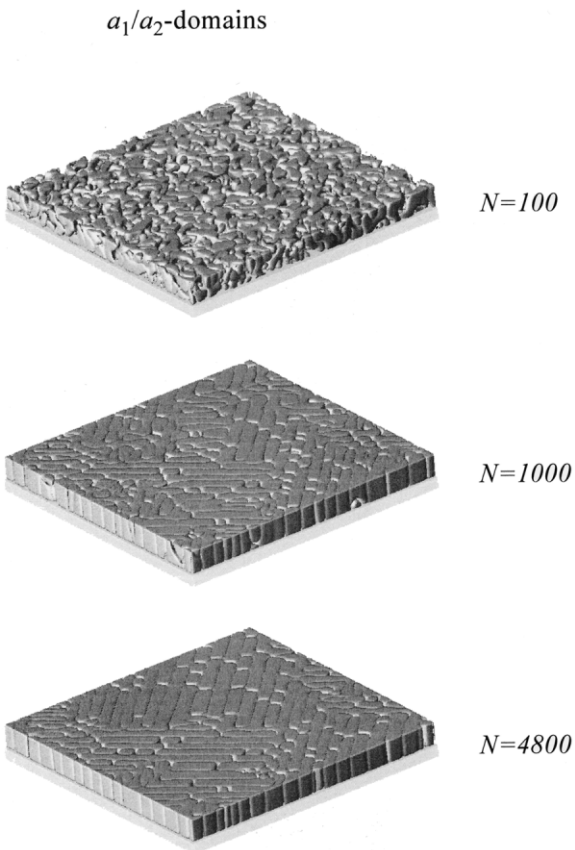


Fig. 10. Temporal evolution of ferroelectric domain morphologies at $\bar{\varepsilon} = 0.012$, $t = N\Delta t$.

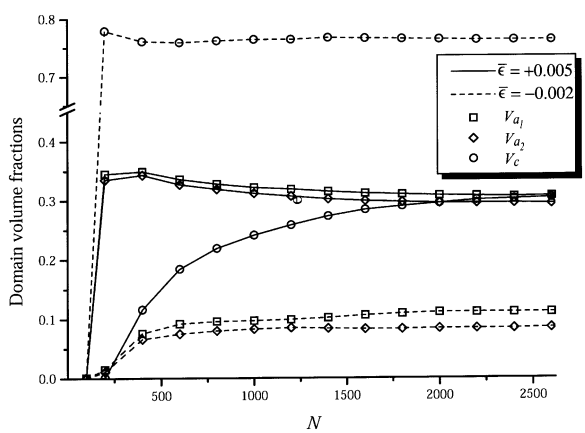


Fig. 11. Domain volume fractions $V_c$, $V_{a1}$ and $V_{a2}$ versus $t = N\Delta t$ at $\bar{\varepsilon} = -0.002$ and $\bar{\varepsilon} = 0.005$.

coexist, even when the volume fraction of $V_c$, is relative large, whereas in prior thermodynamic analyses, simplified domain structures, either $c/a_1/c/a_1$ or $c/a_2/c/a_2$, were assumed, which could not completely accommodate the biaxial constraint along the $x_1$ and $x_2$ axes [35]. Third, we show that the morphologies of *c*-domains are very different from those of *a*-domains (Figs. 4(b) and (c)). The difference in shapes between *a*- and *c*-domains arises from the fact that there are two types of *a*-domains with their tetragonal axes perpendicular to each other. Fourth, when the volume fraction of *c*-domains is small, there are significant number of domains walls between $a_1$- and $a_2$-domains which are perpendicular to the film–substrate interface. Therefore, it is inaccurate to assume that all the domain walls within *c*/*a*/*c*/*a* domain structures are 45° from the film–substrate interface. Finally, our computer simulations show that the domain wall orientations of *c*- and *a*-domains are not exactly along the directions 45° from the film–substrate interface.

In order to examine the consequences of a 2D approximation of a 3D domain structure as used in thermodynamic analyses, we also performed a number of simulations of 2D domain structures. In particular, we chose a system with 128×2×36 grids with periodic boundary conditions along $x_1$ and $x_2$. As a result, the domain structures are two-dimensional along the $x_1x_3$ plane and are uniform along the $x_2$ direction. The results are presented in Table 3 and Fig. 12. In Fig. 12, the black regions represent the $a_1$-domains, the white regions the $a_2$-domains, the gray regions the *c*-domains. The bottom parts in each picture are the substrates. There are two striking differences between our results and those obtained previously using thermodynamic analyses. First, as substrate constraint becomes increasingly tensile, there exist domain structures with all three types of domains, i.e. $a_1/a_2/c$ domain configurations even with a 2D approximation, which is different from Refs. 13–15. Second, the domain walls in a $a_1/a_2/c$ domain morphology are not straight and they deviate significantly from the directions assumed in prior thermodynamic analyses. Therefore, the *c*/*a*/*c*/*a* domain structures with 45° domain walls assumed in prior thermodynamic analyses may not necessar-

Table 3
Volume fractions $V_{a1}$, $V_{a2}$ and $V_c$ versus $\bar{\varepsilon}$ for a 2D approximation

| $\bar{\varepsilon}$ | −0.002 | 0.000 | 0.005 | 0.006 | 0.007 | 0.008 | 0.010 | 0.012 | 0.020 |
|---|---|---|---|---|---|---|---|---|---|
| $V_{a1}$ | 0.168 | 0.234 | 0.381 | 0.416 | 0.445 | 0.418 | 0.399 | 0.410 | 0.435 |
| $V_{a2}$ | 0.000 | 0.000 | 0.000 | 0.003 | 0.044 | 0.261 | 0.499 | 0.517 | 0.561 |
| $V_c$ | 0.789 | 0.712 | 0.516 | 0.460 | 0.350 | 0.132 | 0.000 | 0.000 | 0.000 |

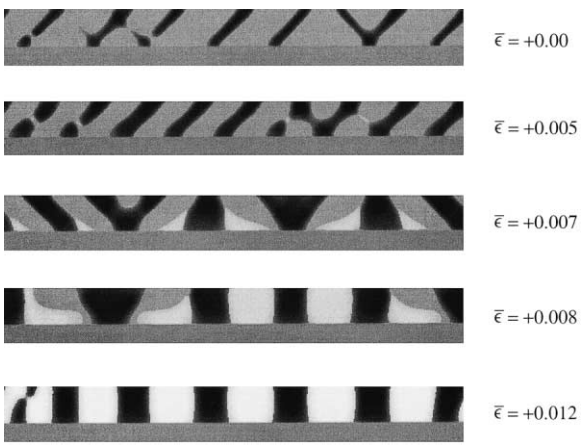


Fig. 12. 2D domain structures for different $\bar{\varepsilon}$.

ily possess the lowest free energy under a given temperature and substrate constraint. Furthermore, with a 2D approximation, even in the case of domain structures containing only $a_1$- and $a_2$-variants, the domain walls between $a_1$- and $a_2$-domains are not exactly perpendicular to the film/substrate interface (Fig. 12).

In our previous work [29], we assumed that the elastic modulus is isotropic, i.e. $C_{11}$=1.746×10$^{11}$ N m$^{-2}$, $C_{12}$=7.937×10$^{10}$ N m$^{-2}$, $C_{44}$=4.762×10$^{10}$ N m$^{-2}$. Table 4 shows the difference in the corresponding volume fractions due to two different $C_{44}$ with one corresponding to an isotropic case and the other cubically anisotropic moduli employed in this work. By comparing the volume fractions in the two cases, it is found that the elastic anisotropy can have an effect on the volume fractions of different domain structures for the same temperature and substrate constraint. Under a compressive or small tensile substrate constraint, the isotropic modulus approximation underestimates the volume fraction of the *c*-domains, whereas under a large tensile constraint, it overestimates the *c*-domain volume fraction.

The present work assumed full coherency between the film and the substrate. Misfit dislocations may be generated to accommodate part of the lattice mismatch between the film and substrate. In principle, the effect of misfit dislocations on the domain volume fractions can be predicted by using an effective substrate lattice parameter taking into account the density of misfit dislocations. However, misfit dislocations are expected to affect also the domain nucleation during a ferroelectric transition and the local domain shapes. Based on the recent advances in developing phase-field models integrating phase and dislocation microstructures [36–38], work is underway to incorporate the misfit dislocations into the phase-field model of domain evolution in ferroelectric thin films.

Table 4
Volume fractions $V_{a1}$, $V_{a2}$ and $V_c$ versus $\bar{\varepsilon}$ for cubic and isotropic elasticity

| $\bar{\varepsilon}$ | −0.006 | | −0.003 | | 0.000 | | 0.003 | | 0.006 | |
|---|---|---|---|---|---|---|---|---|---|---|
| | Cubic | Iso | Cubic | Iso | Cubic | Iso | Cubic | Iso | Cubic | Iso |
| $V_{a1}$ | 0.024 | 0.051 | 0.081 | 0.102 | 0.143 | 0.167 | 0.223 | 0.243 | 0.354 | 0.344 |
| $V_{a2}$ | 0.027 | 0.042 | 0.074 | 0.091 | 0.139 | 0.160 | 0.219 | 0.240 | 0.344 | 0.342 |
| $V_c$ | 0.928 | 0.887 | 0.815 | 0.777 | 0.667 | 0.626 | 0.487 | 0.460 | 0.204 | 0.252 |

Finally, it should be pointed out that the proposed model can be directly applied to ferroelastic phase transformations in thin films as the effect of electric depolarization is ignored in the present formulation. A phase-field model which simultaneously solves the electrostatic and elastic equations is being developed [39]. Our preliminary simulations incorporating the depolarization field show that its effect on the domain structure can be quite significant. The model and results which include the depolarization effect will be reported in a future publication. Therefore, the model and the results presented in this work are applicable to ferroelectric transformations in which the electrostatic energy is considerably less than the typical strain energy. In fact, many experiments showed that the depolarization effects may be insignificant due to the charge compensation by point defects in the ferroelectric films, and the domain formation is controlled by ferroelastic effects and the substrate constraint [34,40].

## 5. Conclusions

A three-dimensional phase-field model was employed to study the ferroelectric domain evolution in elastically anisotropic thin films. An effective method for calculating the elastic strain energy in a constrained anisotropic film was developed. The phase-field model is able to predict not only the volume fractions of domain variants at a given temperature and substrate constraint, but also the detailed domain-wall orientations, surface topology as a result of domain formation, domain shapes and their temporal evolution. It is shown that the domain-wall orientations between *a*- and *c*-domains deviate from the 45 direction from the film–substrate interface as a result of substrate constraint. It is demonstrated that mismatch strain between the film and the substrate can significantly alter the sequence of nucleation and growth, the volume fractions of the three different tetragonal domains. Depending on the mismatch strain and temperature, the domain structures range from a single *c*-domain, to three coexisting variants, $c/a_1/c/a_2$ or $c/a_1/a_2$, to twin domain structures $a_1/a_2/a_1/a_2$. The proposed phase-field model is also applicable to other types of structural phase transformations in thin films.

## Acknowledgements

The authors are grateful for the financial support from the National Science Foundation under Grant No. DMR 96-33719 and DMR-0103354. The computer simulations were performed on Cray-T90 at the San Diego Supercomputer Center and on the Cray-J90 at the Pittsburgh Supercomputer Center.

## References

[1] Lines ME, Glass AM. Principles and applications of ferroelectrics and related materials. Oxford: Clarendon Press, 1977.
[2] Cross LE. Ferroelectric ceramics: tailoring properties for specific applications. In: Ferroelectric ceramics. Basel (Switzerland): Birkhauser Verlag; 1993:1–85.
[3] Arlt G. Ferroelectrics 1990;104:217.
[4] Speck JS, Pompe W. J Appl Phys 1994;76:466.
[5] Kwak BS, Erbil A, Budai JD, Chisholm MF, Boatner LA, Wilkens BJ. Phys Rev 1994;B 49:14865.
[6] Little S, Zangwill A. Phys Rev 1994;B 49:16659.
[7] Foster CM, Li Z, Buckett M, Miller D, Baldo PM, Rehn LE, Bai GR, Guo D, You H, Merkle KL. J Appl Phys 1995;78:2607.
[8] Stemmer S, Streiffer SK, Ernst F, Ruhle M, Hsu WY, Raj R. Solid State Ionics 1995;75:43.
[9] Sridhar N, Rickman JM, Srolovitz DJ. Acta Mater. 1996;44:4097.
[10] Alpay SP, Roytburd AL. J Appl Phys 1998;83:4714.
[11] Roytburd AL. J Appl Phys 1998;83:228.
[12] Roytburd AL. J Appl Phys 1998;83:239.
[13] Pertsev NA, Koukhar VG. Phys Rev Lett 2000;84:3722.
[14] Koukhar VG, Pertsev NA, Waser R. Appl Phys Lett 2001;78:530.
[15] Koukhar VG, Pertsev NA, Waser R. Preprint, 2001.
[16] Wang YZ, Chen LQ. In: Kaufmann EN, editor. Methods in materials research. John Wiley & Sons; 2000.
[17] Nambu S, Sagala DA. Phys Rev 1994;B50:5838.
[18] Hu HL, Chen LQ. J Am Ceram Soc 1998;81:492.
[19] Semenovskaya S, Khachaturyan AG. J Appl Phys 1998;83:5125.
[20] Khachaturyan AG, Shatalov GA. Sov Phys JETP 1969;29:557.
[21] Khachaturyan AG. Theory of structural transformations in solids. New York: Wiley, 1983.
[22] Stroh AN. J Math Phys 1962;41:77.
[23] Ting TCT. Anisotropic elasticity: theory and applications. Oxford University Press, 1996.

[24] Binder K. Ferroelectrics 1981;35:99.
[25] Tilley DR, Zeks B. Solid State Commun 1984;49:823.
[26] Devonshire AF. Phil Mag Suppl 1954;3:85.
[27] Willis JR. Q J Mech Appl Math 1966;18:419.
[28] Lur'e AI. Three-dimensional problems of the theory of elasticity. Interscience Publishers, 1964.
[29] Li YL, Hu SY, Liu ZK, Chen LQ. Appl Phys Lett 2001;78:3878.
[30] Chen LQ, Shen J. Comp Phys Comm 1998;108:147.
[31] Haun MJ, Furman E, Jang SJ, Mckinstry HA, Cross LE. J Appl Phys 1987;62:3331.
[32] Pertsev NA, Zembilgotov AG, Tagantsev AK. Phys Rev Lett 1998;80:1988.
[33] Seifert A, Lange FF, Speck JS. J Mater Res 1995;10:680.
[34] Alpay SP, Nagarajan V, Bendersky LA, Vaudin MD, Aggarwal S, Ramesh R, Roytburd AL. J Appl Phys 1999;85:3271.
[35] Roytburd AL, Alpay SP, Bendersky LA, Nagarajan V, Ramesh R. J Appl Phys 2001;89:553.
[36] Hu SY, Chen LQ. Acta Mater 2001;49:463.
[37] Wang YU, Jin YM, Cuitino AM, Khachaturyan A. Acta Mater 2001;49:1847.
[38] Wang YU, Jin YM, Cuitino AM, Khachaturyan A. Appl Phys Lett 2001;78:2324.
[39] Li YL et al., unpublished (2001).
[40] Foster CM, Pompe W, Daykin AC, Speck JS. J Appl Phys 1996;79:1405.